Tungsten erosion by impurities and redeposition: focus on the magnetised sheath

N. Mellet[1], J.P. Gunn[2], B. Pégourié[2], Y. Marandet[1], C. Martin[1] and P. Roubin[1]

[1] CNRS, Aix-Marseille Univ., PIIM, UMR 7345, 13397 Marseille, France.
[2] CEA, IRFM, 13108 Saint Paul-lez-Durance, France.

E-mail: `nicolas.mellet@univ-amu.fr`

Abstract. The effect of the magnetised sheath on the gross erosion and redeposition of tungsten is examined with an insight on impurity impact energy and angle. A complete treatment of the impact energy is performed leading to a scaling that differs from the usual $2k_BT_i+3Zk_BT_e$ formula. It is found that even if the energy distribution at the sheath entrance strongly differs from this approximation, the discrepancy remains under 20% for the impact energy. The average impact angle of a set of impurities is calculated. The difference between models with and without sheath electric field depends strongly on the charge state and mass of the impurity considered. This can lead, for example in the case of gross sputtering due to impinging W^{12+}, to an underestimation of 3-4 times at $T_e = 25$ eV for very grazing angles. Scalings for high ($n_e > 10^{20}$ m^{-3}) and low ($n_e < 10^{15}$ m^{-3}) density cases are deduced and provide a good estimation of the average impact angle of all impurities. Finally the magnetised sheath is shown to have an effect on the redeposition through two contributions: it increases the prompt redeposition contribution to the total redeposition and constitutes a potential barrier for the ions leaving the surface. A discussion is provided about the optimal width of the simulation domain to capture these effects.

PACS numbers: 52.40.Hf, 52.40.Kh

Submitted to: *Plasma Physics Controlled Fusion*

1. Introduction

In next step fusion devices, erosion of the Plasma-Facing Components (PFCs) is expected to originate mainly from fuel ions during transient events like ELMs (Edge Localised Modes (ELMs)). During inter-ELM operation, however, the impact energy of fuel ions should be below tungsten's sputtering threshold so that the only possible contribution for divertor erosion is due to impurities. In addition to having a lower sputtering threshold than fuel ions, multiply-charged impurities gain more energy as they fall through the sheath potential drop. One origin of the impurities is the erosion of Plasma-Facing Components (PFCs) that will be composed mainly of tungsten (W) and beryllium (Be) in the case of ITER. The concentration of W in the plasma core should be kept as low as possible to guarantee good plasma performance contrarily to Be, for which a higher concentration of Be is tolerated. Another impurity is helium (He), which will be provided by fusion reactions. In this case, the maximum possible charge state is 2, which can result in an impact energy lower than its physical sputtering threshold on W (~ 150 eV). Thus He is not expected to contribute to tungsten erosion during inter-ELM operation. The last source of impurities is the injection of noble gases (Ne, Ar, etc...) or nitrogen (N) in order to spread the power deposition on the divertor and to dissipate it through radiation. In this case, we deal with species that have a low energy threshold (30-50 eV) for physical sputtering of W, that can be multiply charged and can have a substantial concentration in the particle flux that reaches the divertor targets. They can thus be the reason for a non-negligible erosion during inter-ELM operation.

The magnetised sheath is the region between the edge plasma and the surface. It is characterized by the presence of an electric field oriented towards the surface. It is composed of the Debye sheath (DS) that is due to charge conservation and the magnetic pre-sheath (MPS) that comes from the grazing incidence of the magnetic field with respect to the surface. The magnetization parameter ζ has been introduced in a previous work [1] and characterizes the composition of the sheath. It is defined as the ratio between the Larmor radius r_L at the sonic speed for $T_i = 0$ and the Debye length λ_D ($\zeta = r_L/\lambda_D$). In the strongly magnetised case ($\zeta \ll 1$), which is characteristic of low flux regions, the MPS does not exist. In this case the sheath has the width of the DS that is several Debye lengths wide. In the weakly magnetised case ($\zeta \gg 1$), which is characteristic of regions close to divertor strike points, the MPS is several Larmor radii wide. The DS is in this case much smaller than the MPS.

The effect of the sheath electric field is to accelerate the ions toward the surface. It increases their energy but also modifies their impact angle. This has consequences on the gross erosion as different impact energy or angle mean different physical sputtering rate as shown in Figure 1. Several works have already investigated the sheath deflection of impinging particles. In [3] we have shown that the distribution of impact angles is modified by the magnetised sheath and that this effect is larger for impurities than for the main species. Differences in impact angles for various species originating from the

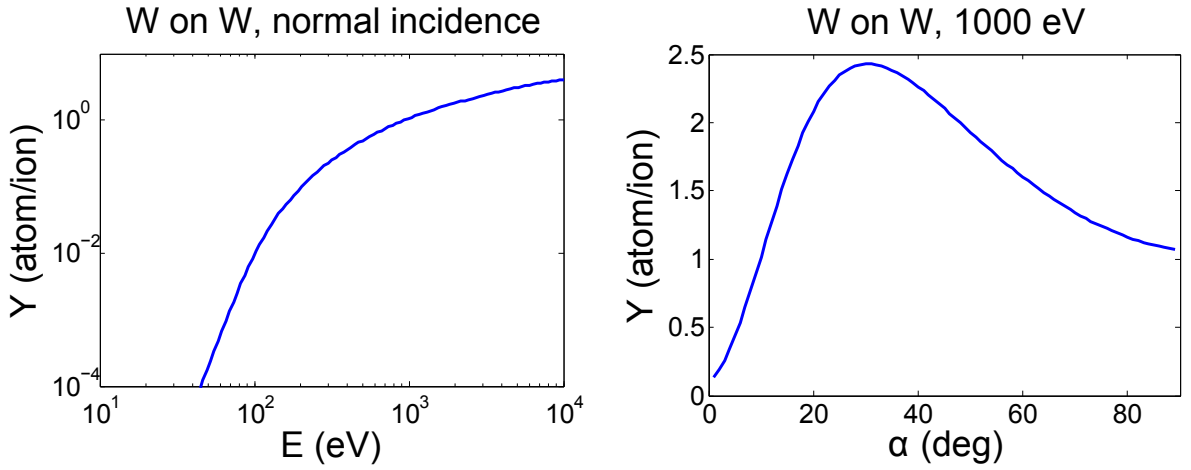


Figure 1. Physical sputtering for W self-sputtering from [2]. Left: energy dependence at normal incidence. Right: Angular dependence at $E = 1000$ eV.

plasma have been emphasized in [4]. Furthermore the impact angle of the promptly redeposited W has also been calculated and is shown to be almost normal, which differs significantly from the long-range transported W. The dependence of the impact angle on the mass and charge state has also been emphasized by other authors [5] that have used a self-consistent modelling of the magnetised sheath electric field. In [6] other self-consistent simulations that include also the collisional region before the sheath have pointed out the presence of two populations that exist as a consequence of collisions. Finally we can cite analytical works where the magnetised sheath effect on the impact angle of particles is calculated. In [7] the sheath electric field is calculated analytically in a fluid framework, which gives the velocity of the impinging flux and thus the impact angle of the main species. The impact angle is also calculated in [8] with an approximated formulation of the magnetised sheath potential.

Redeposition can be investigated by impurity transport codes like ERO [9] or REDEP/WBC [10] that include both long-range and prompt redeposition, which was first described in [11] for tungsten. Recently modelling efforts have largely focused on the effect of improved sheath model, for example with ERO [12]. In [13] simulations of the redeposition have been carried out for two models of ad-hoc magnetised sheath potential [7, 14]. This work has emphasized that only a fraction as low as 10^{-4} of the eroded tungsten atoms manage to leave the sheath in the ELM condition in ITER. It has also shown the strong dependence on the redeposition of the shape of the sheath potential as well as that of the kinetic energy of the ejected tungsten particles. Tskhakaya *et al* [15] have performed self-consistent simulations of the full Scrape-Off Layer (SOL) including effects like temperature gradient drifts and electric field and obtained a global fit for redeposition. The models [13] and [15] have been compared in [16] with respect to their effect on the sputtered W sources. Finally, erosion and redeposition of W have been investigated with the sheath potential calculated during ELMs and compared to experimental data from EAST [17].

From an experimental point of view, several evaluations of prompt redeposition have been attempted. In JET [18] and TEXTOR [?], UV spectroscropy has permitted an in-situ assessement of prompt-redeposition to a minimum of 50%. Dedicated markers in DIII-D [?] and ASDEX-Upgrade [?] have also been used and the results compared to redeposition simulation with ERO and improved sheath models [?, ?].

The aim of this paper is to investigate the different effects of the magnetised sheath on the net erosion. The computations are based on a self-consistent determination of the magnetised sheath potential. First, the impact energy and angle of impurities originating from the SOL are simulated. Second, the redeposition of W atoms eroded by those ions is computed. This work applies mainly to inter-ELM operation even few elements related to ELMs are provided at this end of the paper. It is organized as follows. Section 2 introduces the model for PIC simulations of the magnetised sheath. Section 3 discusses the validity of the usual assumption for the average impact energy ($2k_BT_i + 3Zk_BT_e$) and provides an alternative formula based on simulations. Section 4 treats about the impact angle of the impurities that reach the wall and the consequence on the gross erosion. In Section 5, the simulation of redeposition is investigated. In Section 6, a discussion about additional effects is proposed. Finally the main conclusions are drawn in Section 7.

2. Sheath Model

The simulations are performed with a 1D Particle In Cell (PIC) code [1]. It calculates the trajectories of particles inside the magnetised sheath with the equation of motion:

$$m_p \frac{d\mathbf{u}_p}{dt} = q_p(\mathbf{E} + \mathbf{u}_p \times \mathbf{B}), \tag{1}$$

where the indice $p = b, e, i$ corresponds to the background species (here D), the electrons and the impurity, respectively. The coordinates system is shown in Figure 2. Normalization has been performed so that only a few parameters are required to describe the system:

$$\frac{d\tilde{u}_{p,x}}{d\tilde{t}} = \frac{Z_p m_b}{m_p Z_b}\left(-\tilde{u}_{p,y}\sin\alpha_B\right) \tag{2}$$

$$\frac{d\tilde{u}_{p,y}}{d\tilde{t}} = \frac{Z_p m_b}{m_p Z_b}\left(\tilde{u}_{p,z}\cos\alpha_B + \tilde{u}_{p,x}\sin\alpha_B\right) \tag{3}$$

$$\frac{d\tilde{u}_{p,z}}{d\tilde{t}} = \frac{Z_p m_b}{m_p Z_b}\left(\zeta^2\tilde{E}_z - \tilde{u}_{p,y}\cos\alpha_B\right) \tag{4}$$

where Z_p is the charge state, m_p is the particle mass, α_B the angle of the magnetic field with respect to the surface and $\zeta = \sqrt{m_b n_e/Z_b\epsilon_0}/B$ the magnetization parameter. The sheath electric potential ϕ is computed by Poisson's equation that yields, in its normalized form:

$$\frac{d^2\tilde{\phi}}{d\tilde{z}^2} = \tilde{n}_e - Z_b\tilde{n}_b. \tag{5}$$

The magnetised sheath electric field is calculated self-consistently by Equations (2)-(5) with $p = b, e$ as well as the electron density profile, which is of importance for redeposition simulation as it affects the ionisation. An additional parameter that is the ion to electron temperature ratio $\tau = T_i/T_e$ is required to determine the injection distribution at the sheath entrance (see Figure 2). The total sheath potential drop ϕ_0 is specified by Eq. 2.60 of [19] that depends on the background species mass (m_D) and τ. In what follows we will treat the specific case of $\tau = 1$ that is a good approximation for divertor conditions. $e\phi_0/k_BT_e = -2.89$ is obtained in these conditions and this value will be employed throughout this paper unless explicitly stated. n_e, T_e, T_i are specified at the sheath entrance and vary according to the distance to the wall.

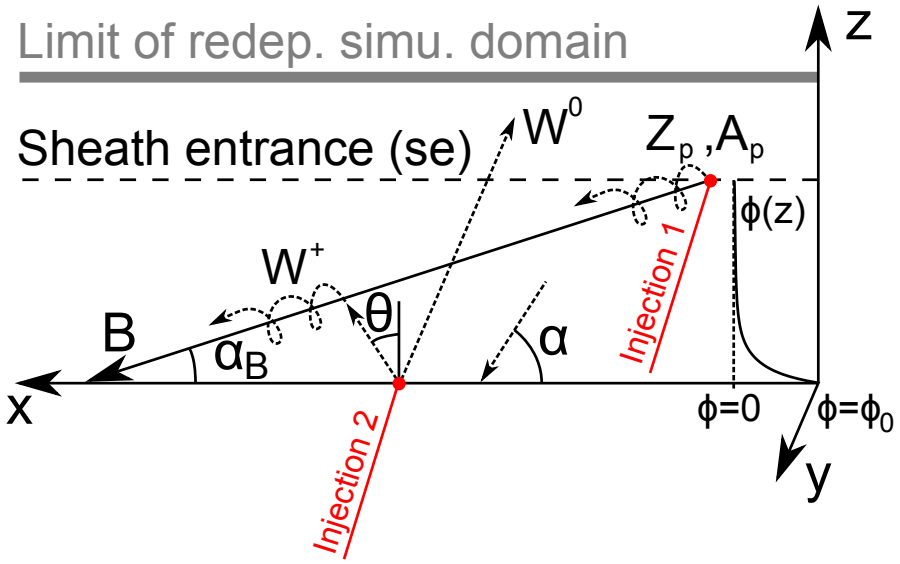


Figure 2. Schematic view of the geometry and the main processes. Particles are injected close to the sheath entrance (Injection 1) for the self-consistent calculation of the magnetised sheath electric field and for the calculation of the impurity trajectories inside the sheath. They hit the surface with an impact angle α. Eroded particles ejected from the wall (Injection 2) can be either redeposited or leave the simulation domain. The domain can extend farther than the sheath entrance.

The simulations of impurities are performed in the magnetised sheath potentials that have been determined for a set of values of α_B and ζ. They are followed as test particles using Equation (2)-(4) with $p = i$. We assume that they do not modify the magnetised sheath potential. This approximation is valid for low concentration of impurities but allows the computation time required to be reduced considerably as self consistent simulations are much longer than considering only test particles and such extensive calculations would be required for each case considered (number and types of impurities, concentrations, etc...). The difference between pure D potential and the potential calculated with impurities is negligible for a concentration of few percents for light impurities (Be, N, Ne) and a concentration of few per thousand for heavier impurities (Ar, W): The larger the charge state, the lower the critical concentration.

Additionally, the heavier the ions the lower the critical concentration as heavy ions spend more time in the sheath due to their lower velocity and affect it more than light ions. Thus computations are made with the assumption of a small impurity concentration (here 0.1%) so that the deuterium background is not disturbed.

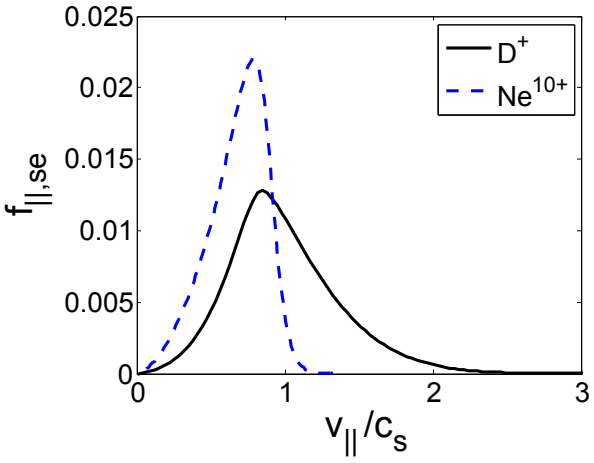


Figure 3. Parallel velocity distribution at the sheath entrance $f_{\|,se}$ obtained at the sheath entrance with the model [21] for D^+ and Ne^{10+} in the case of $\tau = 1$. Velocity is normalized with respect to the sonic speed.

3. Impact energy

Particles are injected at the sheath entrance for the self consistent calculation of the electric field and for the calculation of the impact angles of the impurities from the main plasma (Injection 1 in Figure 2). The injection velocity distribution is especially important as it determines part of the energy distribution at impact. While the velocity of particles perpendicular to the magnetic field is considered to be thermal and is modeled by a Maxwellian distribution, the effect the electric field inside and outside the sheath has to be taken into account to match the Bohm criterion [20] at the sheath entrance for the velocity component parallel to the magnetic field. The method used for each impurity considered separately in a deuterium background is described in [21]. It is a multispecies generalization of the Chung-Hutchinson method [22] and consists of solving the stationary Vlasov's equation for both species and Poisson's equation for isothermal electrons:

$$\left[\frac{\partial}{\partial x_{||}}v + \frac{\partial}{\partial v_{||}}\frac{q_j}{m_j}E(x_{||})\right] f_j(v_{||}, x_{||}) = V\left[f_{j0}(v_{||}) - f_j(v_{||}, x_{||})\right] \tag{6}$$

$$E(x_{||}) = -\frac{k_B T_e}{e n_e(x_{||})}\frac{dn_e(x_{||})}{dx_{||}} \tag{7}$$

where $x_{||}$ and $v_{||}$ are the position and velocity in the direction parallel to the magnetic field, respectively, k_B is the Boltzmann constant and j refers to the species considered. No collisions are considered. The right-hand side term of (6) corresponds to the exchange

at the characteristic frequency V between the populations of the pre-sheath and of the unperturbed SOL flow characterised by a Maxwellian distribution $f_{j0}(v_{||})$. V is chosen to be independent of the velocity and position. No temperature gradients are taken into account and all species are considered to have the same temperature. The interaction between both species is provided by the electric field. The parallel velocity distribution at the sheath entrance is given for Ne^{10+} and compared to D^+ velocity distribution in Figure 3. Although those two species have the same $Z/A = 1/2$ ratio where A is the atomic number, and therefore have the same sonic velocity, their distributions differ however significantly. The larger variance for D^+ than for Ne^{10+} has its origin in the unperturbed Maxwellian SOL distribution whose width depends on the species mass. This result points out that the impurity energies cannot be derived in a simple way.

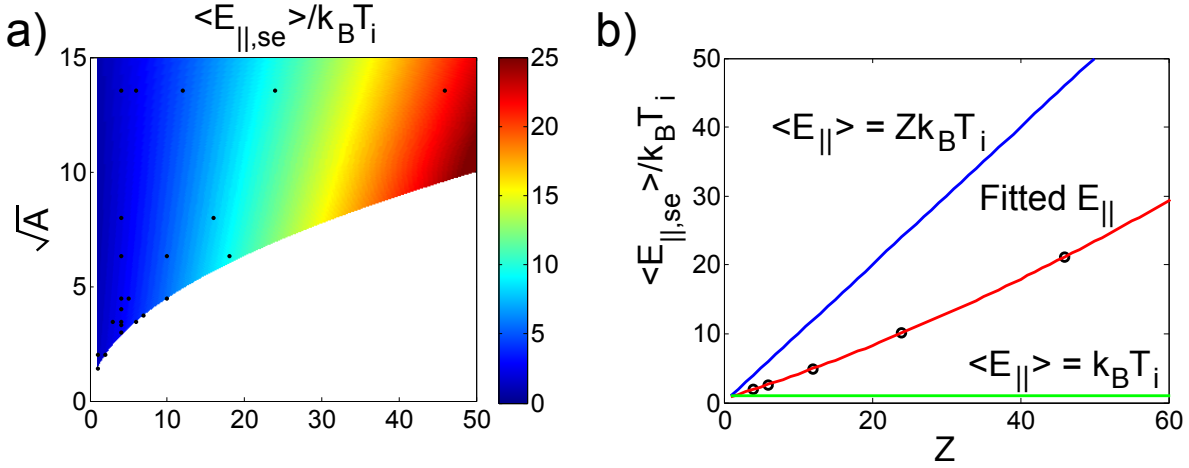


Figure 4. a) Two dimensional fit of the average parallel energy at the sheath entrance. The dots correspond to the simulated species. b) The same fit for $A = 184$ (W) plotted together with two possible approximations: $\langle E_{||}\rangle = k_B T_i$ and $\langle E_{||}\rangle = Z k_B T_i$.

The average parallel energy at the sheath entrance has been studied for a set of impurities including He, Be, C, N, Ne, Ar, W that have been considered at different charge states. This represents 23 cases investigated. The results are shown in Figure 4a, for which a two-dimensional quadratic fit has been performed. As expected, an increase of the parallel average energy at the sheath entrance is observed when the charge state is raised. The dependence is however not linear and does not correspond to any of the approximations that could be made at the sheath entrance ($k_B T_i$ or $Z k_B T_i$). This is displayed in Figure 4b for the case of tungsten as a function of the charge state. Another observation is that the energy is reduced when the mass is increased. If inertia was the only reason for the difference between species, the average energy would be the same for a given mass and would scale linearly with the charge state. In fact the acceleration of particles before they reach the sheath entrance is a complex combination between the plasma electric field and the interaction with the unperturbed SOL plasma that tends to bring the distribution back to a Maxwellian.

In order to determine the impact energy, test particle simulations of the sheath

Table 1. Fit coefficients for the average parallel velocity at sheath entrance given for different values of τ.

τ	f_{00}	f_{10}	f_{01}	f_{20}	f_{11}	f_{02}
0.5	0.63E0	-1.39E-1	6.40E-1	5.37E-3	-1.43E-2	2.05E-3
1	1.13E0	-1.44E-1	5.48E-1	7.24E-3	-1.50E-2	2.26E-3
2	2.10E0	-1.33E-1	4.46E-1	6.73E-3	-1.39E-2	2.24E-3
5	5.08E0	-1.04E-1	3.20E-1	5.99E-3	-1.19E-2	2.11E-3

effect for all species have been performed for different values of α_B and ζ. The average energy increase in the sheath does not depend on any of those parameters and simply corresponds to the magnetised sheath potential drop. We obtain the following relation for the average impact energy:

$$\langle E_{imp} \rangle = [1 + f(A,Z)]\, k_B T_i - 0.5 \log \left[2\pi \frac{m_e}{m_D} (1+\tau) \right] Z k_B T_e \tag{8}$$

where

$$f(A,Z) = f_{00} + f_{10} A^{1/2} + f_{01} Z + f_{20} A + f_{11} A^{1/2} Z + f_{02} Z^2 \tag{9}$$

The first term of (8) corresponds to the perpendicular thermal velocity. The second term corresponds to the average parallel velocity calculated in this section. It is given as a second order polynomial and the coefficients are provided in Table 1. Finally the third term corresponds to the potential drop in the magnetised sheath.

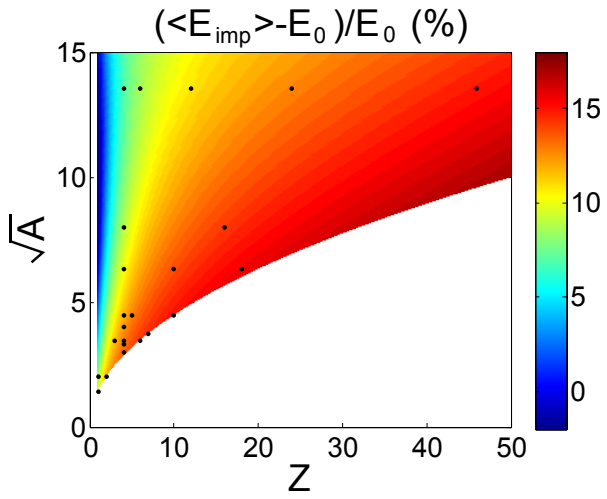


Figure 5. Difference between the average impact energy obtained with the multispecies Vlasov simulations and the analytical formula $2k_BT_i + \phi_0 Z k_B T_e$. The dots correspond to the simulated species.

The average energy obtained is compared in Figure 5 to the usual impact energy formula ($E_0 = 2k_BT_i + \phi_0 Z k_B T_e$) in the case $T_i = T_e$. Instead of using the usual value $\phi_0 = 3$, the calculated potential drop was employed so that the discrepancy between the two model has its origin only in the parallel average energy. Figure 5 shows that the

error $(\langle E_{imp}\rangle - E_0)/E_0$ is of the order of $\sim 0-20\%$. The $2k_BT_i + \phi_0 Zk_BT_e$ formula is in good agrement with the simulated value for low charge state. A difference of $\approx 10\%$ is however visible for low mass ions. For all masses, when the charge state is increased, the difference quickly raises to $\approx 10\%$. For larger charge state, the slope is reduced due to the contribution of the acceleration in the sheath that increases linearly with the charge state and that is taken into account in the same manner in E_0 and $\langle E_{imp}\rangle$.

4. Impact angle and gross erosion

The impact of ions on the wall is characterised by a distribution of impact angle α (see Figure 2). In this section, we focus only on the average value $\langle\alpha\rangle$ so that the effect of the sheath parameters on the impact angle can be addressed clearly. Figure 6 shows the average impact angle for the main species (D^+, top) and for an example of impurity (W^{12+}, bottom). The values calculated by taking into account the magnetised sheath (left) and the difference with the ballistic model (right) are plotted. The ballistic model corresponds to the case without sheath and where only the cyclotron motion is retained. In both cases two regions can be distinguished: at low density ($\zeta \ll 1$) the magnetised sheath reduces the impact angle, while at high density ($\zeta \gg 1$) the magnetised sheath increases the impact angle. The sheath deflection is larger for the impurity considered here, and in general for all impurities, than for the main species. For example, the maximum discrepancy at high density between both models reaches about 24° for W^{12+} and only 10° for D^+. A second difference is that the transition where the sheath starts to increase the impact angle happens at much lower densities for W^{12+} than D^+. At $\zeta = 2$ for example, the sheath would have the effect to increase strongly the impact angle for W^{12+} but almost no effect or even a decrease of the impact angle is expected for D^+.

In order to quantify and understand better the effect of the magnetised sheath on the impact angle, we plot in Figure 7 the impact angle in the asymptotic cases corresponding to the low and high electron density limits for the set of impurities already considered in Section 3. As it is highly expensive in terms of computation for very large or very small values of ζ we limit ourselves to $\zeta = 150$ for the high density case and to $\zeta = 0.1$ for the low density case. When in most cases the impact angle does not vary anymore at $\zeta = 0.1$, slight modification of a few degrees can occur at $\zeta = 150$. This can be observed in Figure 6 where the contour lines are vertical at $\zeta = 0.1$ but still oblique at $\zeta = 150$.

At low density, $r_L \ll \lambda_D$ and the particles have an almost circular gyromotion around the magnetic field lines: the electric field variation during a gyration plays only a minor role on them (see Eq. 3 with $\zeta \ll 1$) and they are said to be strongly magnetised. They undergo the sheath potential drop that will mainly accelerate them in the direction parallel to the magnetic field. In this case, their impact angle can be approximated by a function of $\langle v_\perp\rangle/\langle v_{||}\rangle$: $\langle\alpha_{sh}\rangle \sim f(\langle v_\perp\rangle/\langle v_{||}\rangle) = f(\sqrt{1/A}/\sqrt{Z/A}) = f(\sqrt{1/Z}) = f(1/Z)$. It is in good agreement with what is observed in Figure 7a.

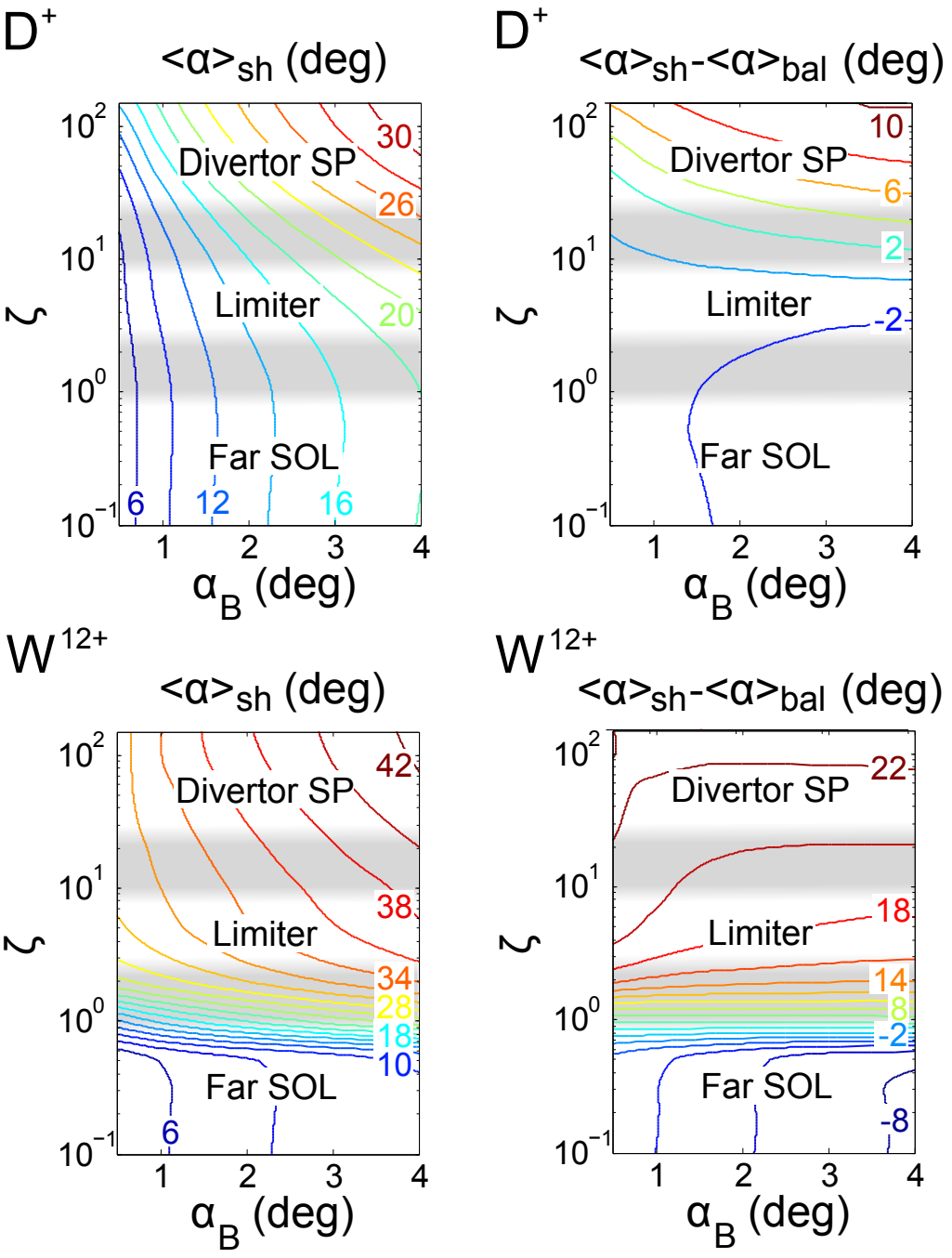


Figure 6. Average impact angle with the sheath (left) and the difference with the ballistic model (right) for D^+ (top) and W^{12+} (bottom). In order to guide the eye, the graph has been separated in three regions with no strict boundaries: divertor strike points ($n_e \gtrsim 10^{19}$ m^{-3}), limiter (10^{17} m$^{-3} \lesssim n_e \lesssim 10^{19}$ m^{-3}) and far SOL ($n_e \lesssim 10^{17}$ m^{-3}).

At high density, $r_L \gg \lambda_D$ and the particles are strongly deflected towards the wall during their last gyration where they experience a strong variation of the sheath electric field. In this case, an increase of the impact angle is expected and observed. To find a scaling, we consider the impact angle to be a function of the distance covered

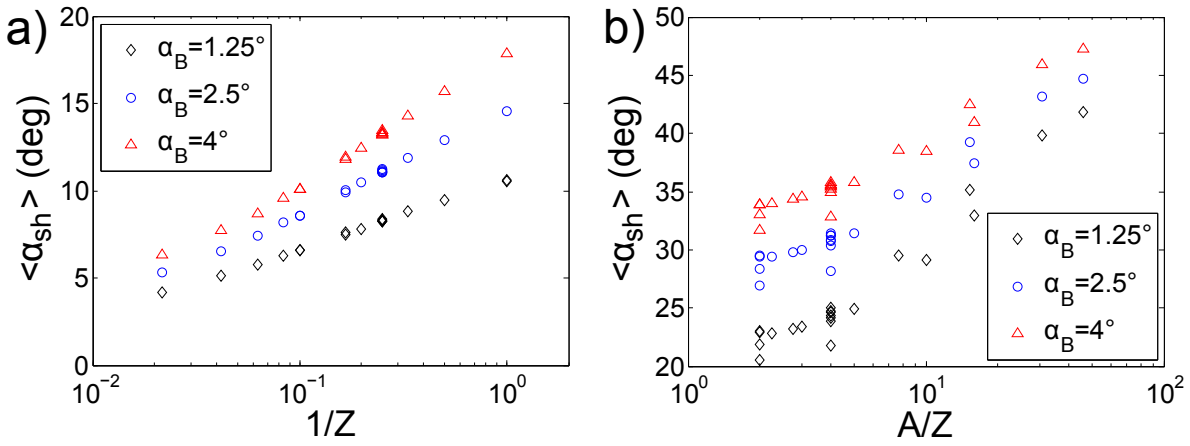


Figure 7. a) Average impact angle at low density ($\zeta = 0.1$). b) Average impact angle at high density ($\zeta = 150$).

during the last gyration towards the wall that is approximated by $\langle r_L\rangle\langle v_{||}\rangle/\langle v_\perp\rangle \sin\alpha_B$. The following dependence is obtained: $\langle\alpha_{sh}\rangle \sim f(\langle r_L\rangle\langle v_{||}\rangle/\langle v_\perp\rangle) = f(A\langle v_{||}\rangle/Z) = f(\sqrt{A/Z}) = f(A/Z)$. Some differences with this scaling are observed in Figure 7b but it gives the main trend.

Data corresponding to three different values of α_B are displayed in both pictures. The difference between them is larger than the difference between the values of α_B. This exists already in the ballistic case where the impact angle difference is larger than the difference in α_B. In the low density case (Figure 7a), $\langle\alpha\rangle$ tends towards α_B when Z is increased as the acceleration in the direction parallel to the magnetic field gets much larger than the perpendicular velocity, reducing at the same time the discrepancy between the three curves.

It is also possible to plot the effective gross sputtering yield as a function of ζ and α_B. It corresponds to the sputtering yield Y (number of ejected atoms per impinging ion) at the average impact angle. Figure 8 displays this quantity for the sheath and ballistic models in the case of W^{12+} impacting the surface at 1000 eV. Given the fact that we have $\tau = 1$, this is satisfied when $T_i = T_e = 25$ eV. The angular dependence of the self-sputtering of W is provided in Figure 1.

In the case of the ballistic model (Figure 8 (middle)) the effective sputtering yield increases with α_B. This is due to the fact that the average impact angle varies from $\langle\alpha_{bal}\rangle = 6.9°$ at $\alpha_B = 0.5°$ to $\langle\alpha_{bal}\rangle = 18.0°$ at $\alpha_B = 4.0°$, which lies in the monotonically increasing part of $Y(\langle\alpha\rangle)$ (see Figure 1). In the case of the sheath model (Figure 8 (left)) strong variation of the average impact angle ($\langle\alpha_{sh}\rangle = 10° \rightarrow 28°$) leads to strong variation of $Y(\langle\alpha_{sh}\rangle)$ between $\zeta = 0.5$ and $\zeta = 2$. Above $\zeta = 2$ on the contrary, $Y(\langle\alpha_{sh}\rangle)$ keeps almost the same value for all parameters. While $\langle\alpha_{sh}\rangle$ still varies above $\zeta = 2$, however moderately, the sputtering coefficient is close to the maximum (see Figure 1) where it depends only slightly on the impact angle.

We finally compare the effective sputtering yield of the cases with and without the sheath (Figure 8 (right)). The place where both models have the same $\langle\alpha\rangle$ is

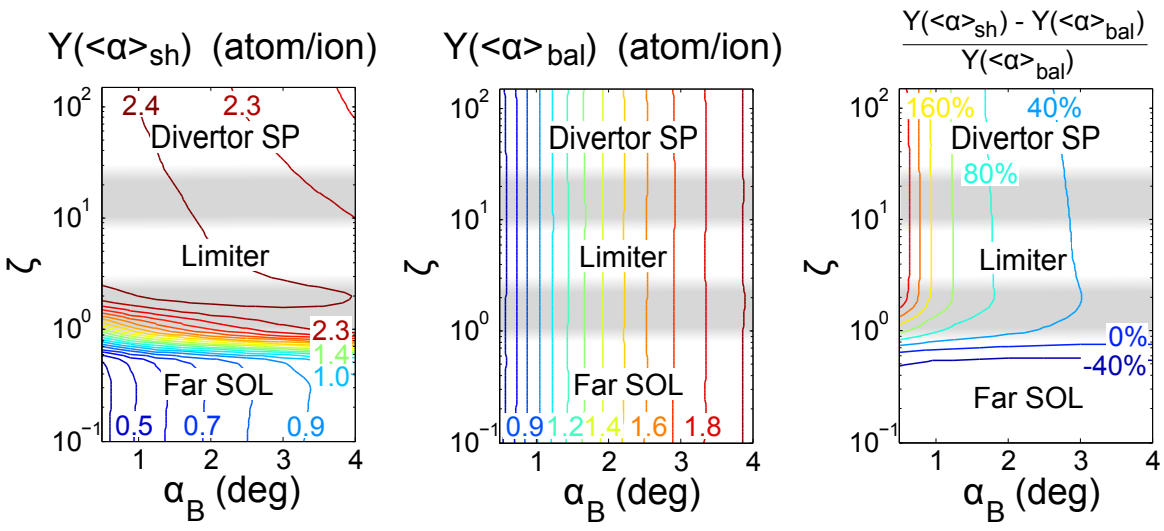


Figure 8. Effective gross sputtering yield due to impinging W^{12+} in the case of the sheath model (left), ballistic model (middle) and the relative difference between both of them.

situated around $\zeta = 0.8$ and corresponds to the same $Y(\langle\alpha\rangle)$ (labelled as 0% on Figure 8 (right)). Below this value the ballistic model has a larger average impact angle and a larger sputtering ($< 0\%$). Above this value it is the sheath model that has a larger average impact angle and a larger sputtering ($> 0\%$). At very low angle, $Y(\langle\alpha\rangle)$ with the sheath model can be more than three times the value of the ballistic model.

5. Redeposition

5.1. Redeposition model

In order to evaluate the net erosion, redeposition must be determined.. Here we focus on the local redeposition (i.e. when the particles do not leave the magnetised sheath). To simulate this contribution, we use again the test particle method with the set of sheath potentials, electron densities and temperatures calculated previously. Particles are ejected from the surface (Injection 2 in Figure 2) with a cosine angular distribution and a Thompson energy distribution [23]. Those distributions are valid in the case of impact by particles whose energy is much above the physical sputtering threshold. At lower energy they tend to become anisotropic (see for example [24, 25, 26]). The method gives however a good indication of the behavior of local redeposition. Considering an energy distribution has already been proven to have a non negligible effect in [27] and shows that redeposition is increased at low density and decreased at high density in comparison to the monoenergetic case.

The Thompson energy distribution can be written as:

$$f(E) \propto \frac{E}{(U_S + E)^3} \left(1 - \sqrt{\frac{E + U_S}{E_{max} + U_S}}\right) dE \tag{10}$$

with a cut-off given by the maximum ejection energy E_{max} and where U_S is the surface binding energy ($U_S = 8.68$ eV for W). To determine E_{max}, we use the following relation given by Mousel et al [28] and based on the calculation of the sputtering threshold performed in [29]:

$$E_{max} = \gamma \langle E_{imp} \rangle \left(\frac{m_1 + 2m_2}{2m_1 + 2m_2} \right)^6 \tag{11}$$

where $\gamma = 4m_1m_2/(m_1 + m_2)^2$, E_{imp} is the average impinging ion energy, m_1 is the impinging ion mass et m_2 is the sputtered atom mass. Eq. 11 has been derived for $m_1 \leq m_2$ and has been successfully compared with experimental data in the case of tungsten [28]. We can also evaluate the average ejection energy from Eq. 10 :

$$\begin{aligned} E_{avg} &= \frac{\int_0^{E_{max}} E f(E) dE}{\int_0^{E_{max}} f(E) dE} \\ &= U_S \frac{\ln 1/\Gamma + (2/3\,\Delta^2 - 1/2)\,\Gamma^2 + (8/3\,\Delta + 2)\,\Gamma + 16/3\,\Gamma^{1/2} - 41/6}{(2/3\,\Delta^2 + 1/2)\,\Gamma^2 + 1/3\Gamma - 4/3\,\Gamma^{1/2} + 1/2} \end{aligned} \tag{12}$$

where $\Gamma = \frac{1}{E_{max}/U_S + 1}$ and $\Delta = \frac{E_{max}}{U_S}$.

Once the particle is ejected, it can be ionised, which is implemented through a Monte Carlo method. The probability of ionisation is given by the ADAS database [30]. Only electron impact ionisation is taken into account. The ionisation rate depends on the electron temperature and density. The ionised particles feel the sheath potential and can be ionised a few times.

Six parameters are required to describe local redeposition conditions. First the three parameters that describe the magnetised sheath electric field have to be retained (τ, ζ, α_B). We know also that the electron impact ionisation rate depends on the electron temperature T_e, which is our fourth parameter. The fifth parameter is the electron density provided in the work by ζ as the magnetic field norm is fixed to $B = 4.2$ T. The last parameter is characteristic of the impinging ion species and affects the ejected tungsten energy distribution. The ejection energy distribution can be characterized by two quantities: its maximum and its average value. Given the fact that we deal with a fixed value of U_S, they are related to each other and only one of them is required. As far as E_{max} depends linearly on $\langle E_{imp} \rangle$ that scales as $k_B T_e$, the more straightfoward parameter that can be used is $E_{max}/k_B T_e$.

5.2. Magnetised sheath and simulation domain width

Several mechanisms can lead to redeposition and are schematized in Figure 9. The first contribution is the prompt redeposition where the ions return to the surface during their first Larmor gyration. The second and third contributions, which we will refer to as long-range redeposition, concern the atoms that are ionised further in the sheath depending on the projection of the sputtered atom velocity along the magnetic field. If the projected velocity is oriented towards the wall, the ion will return in all cases to the wall. If the projected velocity is oriented towards the plasma, the ion may exit the sheath

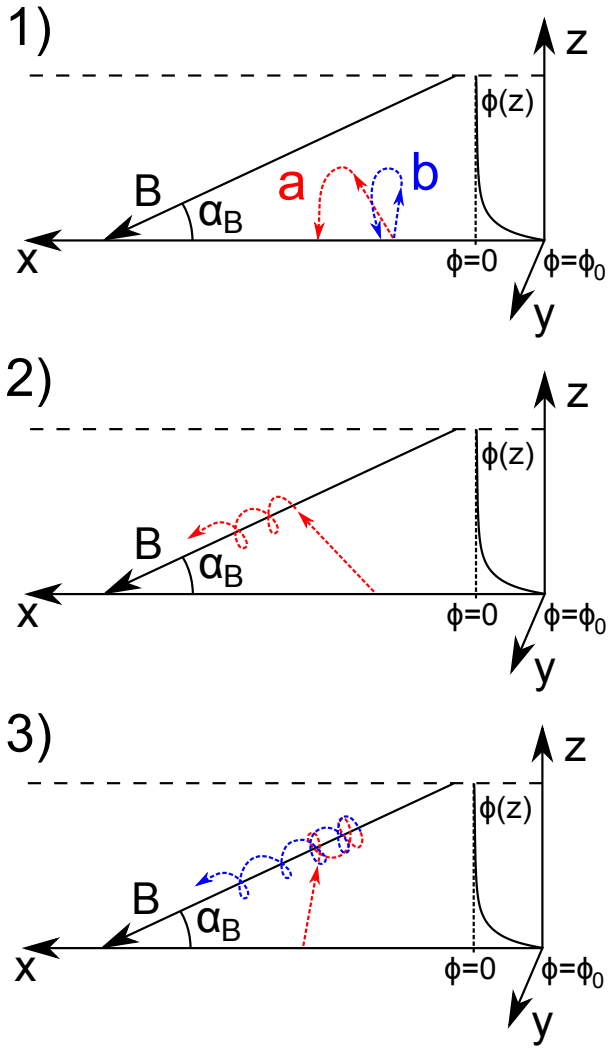


Figure 9. Mechanims involved in local redeposition: 1) Prompt redeposition during first Larmor gyration, 2) Long-range redeposition when the velocity projected along the magnetic field is oriented towards the wall, 3) Long-range redeposition when the velocity projected along the magnetic field is oriented away from the wall.

if it has a sufficient energy to overcome the sheath potential. The same distinction has been made for the prompt redeposition (towards the wall (1a) and towards the plasma (1b)).

On the one hand, contributions 1a and 2 depend on the simulation domain width. As all ionised particles are redeposited, redeposition corresponds to the ionisation probability inside the simulation domain that is related to the sheath width. On the other hand, contributions 1b and 3 depend only on the sheath electric potential. Far from the wall where the sheath electric field is negligible, all ions are able to escape and the simulation domain width does not change redeposition.

In order to simulate the magnetised sheath effect on redeposition, it is important to consider the extension of the simulation domain properly. A too wide domain

would mean an artificial increase of the ionisation probability and thus a too large redeposition. A too small domain would mean that not all the effect of the sheath electric field would be taken into account and thus a too small redeposition. A possible application of the redeposition model is the implementation in tokamak edge codes. In edge fluid codes like SolEdge2D [32], B2.5 [33] or EDGE2D [34], sheath physics provides boundary conditons for the plasma fluid solver (the computational grid stops at the magnetic sheath entrance), that is the Bohm criterion is supposed to hold there. The ion impact angle is determined in the EIRENE Monte Carlo code [35], assuming a maxwellian distribution fonction, shifted by the sound speed in the parallel direction and with the kinetic energy gained in the sheath added in the direction of the surface normal. In Soledge2D-EIRENE, an improved description, based on tables made with the same PIC code as used here, has been added [16]. A first attempt to account for prompt redepostion in a similar fashion has been presented in [36], on the basis of tables published by Chankin et al [13]. This amounts to a correction of sputtered fluxes representing local redeposition. The results presented in this work will allow for a more consistent implementation, treating sheath physics effects with the same tools (that is, average impinging ions energy and angle, together with prompt redeposition fractions).

In order to account for local redeposition, two possibilities exist wether the magnetised sheath is considered to have an zero or finite extension in the edge code. In the first case, which corresponds to today's situation, two conditions are required: (1) the simulation should include all the redeposition due to ionisation until the sheath edge, (2) the simulation should include the total contribution due to the sheath electric field. In the second case, considering finite extension means to retain the elements not computed by EIRENE: gyration motion (contribution 1a) and sheath electric field (condition 2).

The extension of the simulation domain is strongly linked to the sheath width. We start consequently by evaluating the latter with respect to the magnetization parameter ζ and to the ion to electron temperature ratio τ. At low electron density, it scales like the Debye length as background ions span only a small area during their cyclotron motion and do not tend to extend the sheath width. At high electron density it scales like the background ions Larmor radius as the MPS has a larger extension than the DS in that case. The average Larmor radius of D^+ is calculated considering its average energy between the sheath entrance and the wall: $r_{LD^+} \sim c\sqrt{(m_i/eB^2)(k_BT_i + k_BT_i + \phi_0 k_BT_e)} = c\sqrt{(m_i/eB^2)(2\tau + \phi_0)k_BT_e}$, where c is a fit factor. A possibility is to consider the low and high density cases as linearly independent and to take their norm as the sheath width. The following relation is obtained:

$$L_{sh,f_\phi} = L_{D,f_\phi}\sqrt{1 + 0.207\,(2\tau + \phi_0)\zeta^2}, \tag{13}$$

where L_{sh,f_ϕ} is the distance to the wall where the potential jump reaches a fraction f_ϕ of the total potential drop ϕ_0 and L_{D,f_ϕ} is a parameter proportional to the Debye length. c has been set to 0.207 so that $L_{sh,f_\phi} = L_{D,f_\phi}\sqrt{1+\zeta^2}$ for $\tau = 1$. The sheath width is then defined as $L_{D,1.0}$. Equation 13 is supposed to be valid for f_ϕ close to unity. In order to

check the consistency of such an expression, we use the sheath width obtained by the PIC code. The quantity that is checked is $L_{sh,0.9}$ e.g. the location where the potential has already dropped from 90% of its overall value. It is not possible to determine $L_{sh,1.0}$ directly as it depends on the simulation domain used for self-consistent sheath calculation. Figure 10 shows a comparison between the value of $L_{sh,0.9}$ determined by simulations and Eq. (13) where we have used $L_{D,0.9} = 4.28\lambda_D$ for $\tau = 1$ (left) and $\tau =$ 0.5, 2 and 5 (right). A good agreement is obtained and validates the use of Eq. (13). A value of $L_{D,1.0} = 10\sqrt{2}\lambda_D$ is finally obtained with the PIC code by considering the optimal location for particle injection for the case $\tau = 1$, on which the rest of the paper will focus.

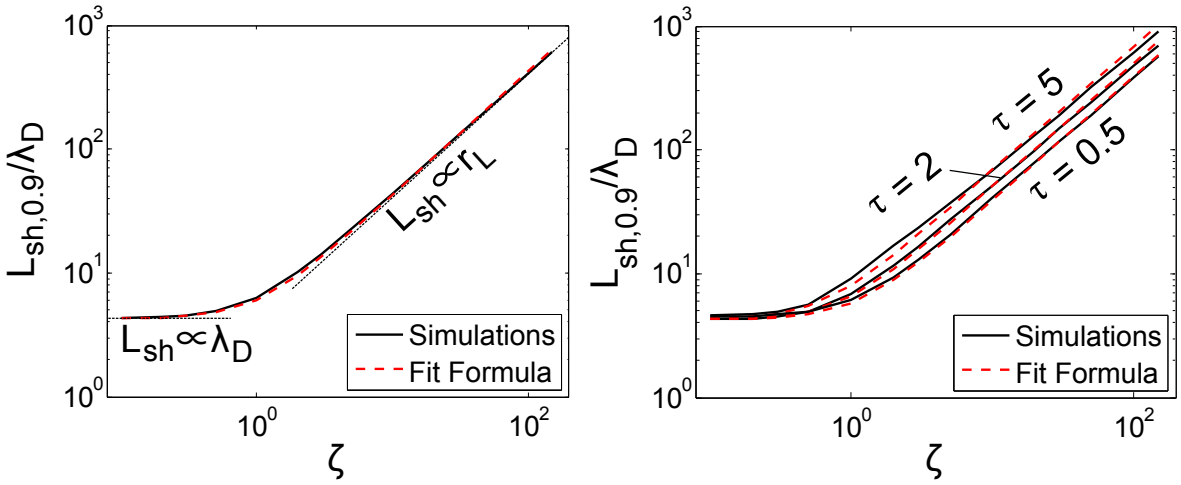


Figure 10. $L_{D,0.9}$ determined with the PIC code (black) and with the fit formula (13) for $L_{D,0.9} = 4.28\lambda_D$ (red). Left: $\tau = 1$. Right: $\tau = 0.5$, 2 and 5.

The sheath width being evaluated, we concentrate now on the estimation of the optimal simulation domain extension for redeposition simulation. We introduce L_{simu} and L_S that are the equivalent of $L_{sh,1.0}$ and $L_{D,1.0}$, respectively but for the simulation domain ($L_{simu} = L_S\sqrt{1+\zeta^2}$ for $\tau = 1$) . Following condition (1) given above, $L_S \geq L_{D,1.0}$. In order to verify if condition (2) is satisfied, e.g. if all the effects of the sheath electric field are taken into account, the non-redeposition fraction (the ratio between the number of particles that leave the simulation domain and the total number of ejected atoms) are displayed in Figure 11 for the contributions that depend only the magnetised sheath width (1a and 2) and those that are also influenced by the sheath electric field (1b and 3) in the case of W ejected by W^{12+} at $T_e = T_i = 25$ eV for $B_0 = 4.2$ T. It is not surprising to see that the particles whose velocity projection is like **B** lead to more redeposition than those in the opposite direction as when they are ionised they always return to the wall. Additionally the non-redeposition fraction is decreased by increasing the simulation domain for contributions 1a and 2 (Figure 11(left)). If we now focus on the contributions that are influenced by the sheath electric field (1b and 3, Figure 11(right)), the non-redeposition fraction converges by increasing the simulation

domain and the final value is attained around $L_S = 20\sqrt{2}\lambda_D$. This value stands twice above the extension of the sheath electric field (until $L_{D,1.0} = 10\sqrt{2}\lambda_D$). A possible explanation is the case of atoms that would exit the sheath at $z = 10\sqrt{2(1+\zeta^2)}\lambda_D$ and be ionised outside of this region. If $L_S = 10\sqrt{2}\lambda_D$, those particles are considered to have escaped the sheath. If $L_S = 20\sqrt{2}\lambda_D$, a possibility exists that the gyrocenter of the new ions is inside the sheath and that the particle can still be redeposited.

In order to satisfy the two conditions required for the simulations of sheath effects on redeposition, different simulation domains should be employed for the particles whose velocity projection along **B** are oriented towards the wall or towards the plasma. For contributions (1a) and (2), it should extend until the sheath edge ($L_{simu} = 10\sqrt{2}\lambda_D$) so that redeposition due to ionisation is taken into account in the region not treated by edge codes. For contributions (1b) and (3) it should extend until where the total effect of the electric field is retained ($L_{simu} = 20\sqrt{2}\lambda_D$).

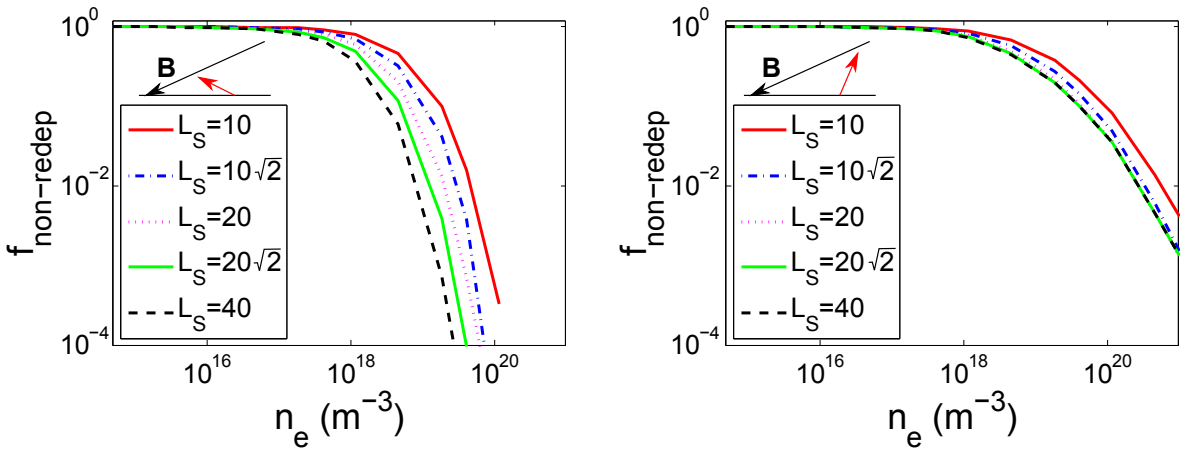


Figure 11. Non-redeposition fraction of W ejected by W^{12+} at $T_e = T_i = 25$ eV for $B_0 = 4.2$ T and $\alpha_B = 3°$ with the velocity projection in the direction similar (left) as and opposite (right) to the magnetic field.

5.3. Effect of the sheath on redeposition

The evaluation of the magnetised sheath effect on the redeposition is performed in the case of W ejected by W^{12+}. The electron and ion temperatures are $T_e = T_i = 25$ eV, $B = 4.2$ T with an angle with respect to the surface of $\alpha_B = 3°$. We first compare the non redeposition fraction with and without the magnetised sheath (e.g. the ballistic case) in Figure 12a. The sheath tends to increase strongly the redeposition as it attracts the ions towards the surface and constitutes a potential barrier for ions leaving the sheath. The number of particles that manage to escape is still significant at $n_e = 10^{21}$ m^{-3} without the sheath electric field (more than 20%).

The contribution of the different mechanisms is displayed in Figure 12bc. First we see that contribution 3 does not exist in the case without sheath. This is due to the fact that this contribution purely originates from the sheath electric field. A larger

contribution of prompt redeposition in the sheath case than in the ballistic case is also observable leading to a very reduced ratio of long-range redeposited ions. This is consistent with the fact that the sheath attracts the ions towards the wall making them lose their circular trajectories and thus increasing the probability of an impact during the first gyration. At large densities the long-range contributions disappears even almost completely.

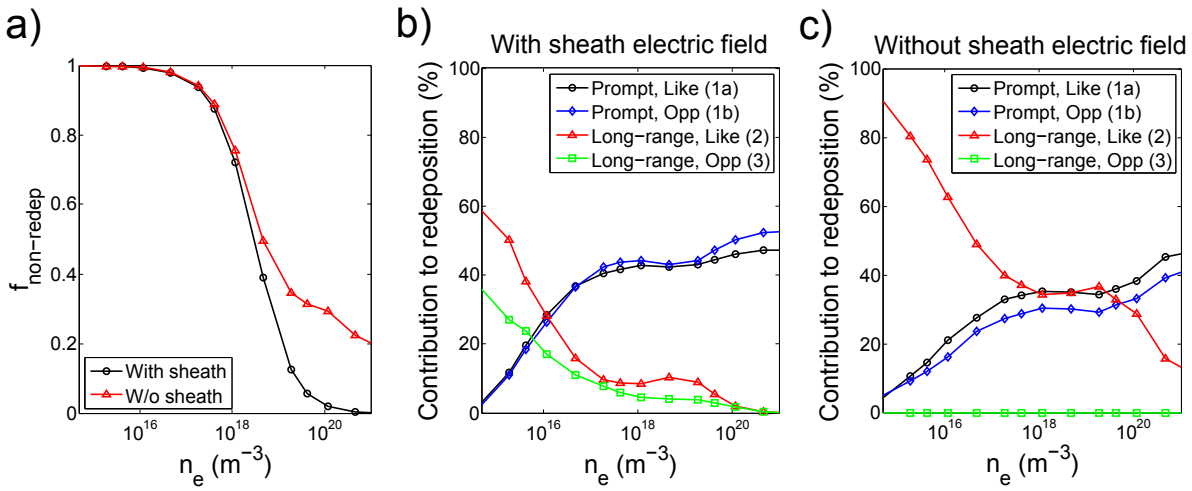


Figure 12. a) Non redeposition fraction with ou without the electric sheath potential. b) Importance of the contributions to the redeposition with the sheath. c) Importance of the contributions to the redeposition without the sheath. W ejected by W^{12+} at $T_e = T_i = 25$ eV for $B = 4.2$ T.

We compare then the two contributions of prompt redeposition. We see that almost everywhere contribution 1b is larger than contribution 1a. The reason is that the number of atoms ejected in the direction opposite to the magnetic field is larger than the number of atoms ejected in the same direction because of the magnetic field **B** inclination (57% of ejected atoms have a velocity projection along **B** oriented towards the plasma).

The effect of E_{max}/k_BT_e and of T_e on the non-redeposition fraction is displayed in Figure 13 for $\zeta = 30$, $B = 4.2$ and $\alpha_B = 3°$. This means a fixed density of 4.21×10^{19} m^{-3}. To guide the eye, E_{max}/k_BT_e calculated from Eq. 11 for several impurities at $\tau = 1$ is plotted. The greyed region corresponds to ELMs and is only given as an indication. According to [37] that refers to the free-streaming model [38, 39], most of the energy of the electrons is transferred to the ions during ELMs. The magnetised sheath potential drop would not be modified by ELMs as far as the electron temperature at the target is not modified from the inter-ELM situation. As a first approximation, the redeposition model is applied in the same way as in inter-ELM conditions considering the different impact energies of the ions. The greyed region is determined by considering an ion energy above 1 keV at the sheath entrance. Note that the sheath width could be substantially increased according to Equation 13 considering the possible large value of T_i/T_e. The electric field could be reduced at the same time. Note that an electron temperature growth during ELMs has been observed in TCV [40]. A raise of the potential drop has

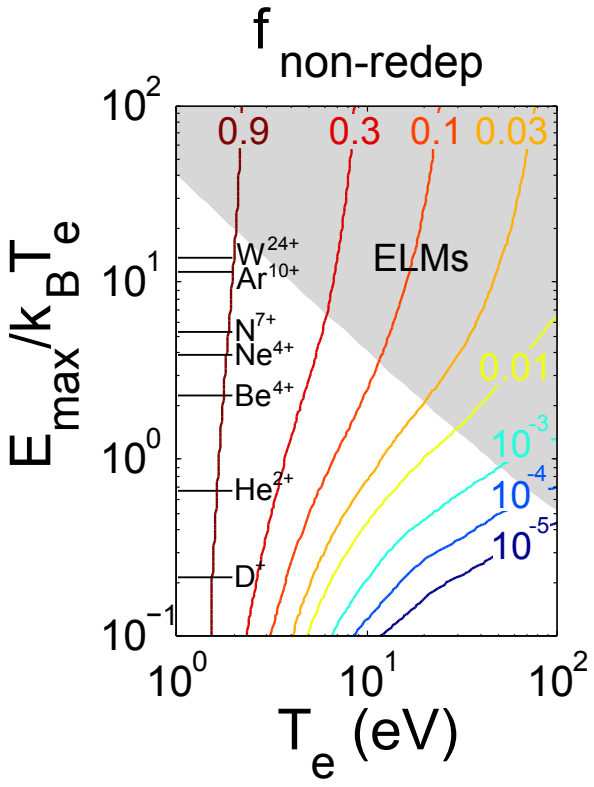


Figure 13. Scan of $f_{non-redep}$ as a function of T_e and E_{max}/k_BT_e. Several impurities are represented on the graph for $\tau = 1$. The ELMs region corresponds to ion energy at the sheath entrance larger than 1 keV.

also been obtained by sheath simulation during ELMs [17]. This leads to an increased redeposition in comparison to the prediction based on the free-streaming model, which could be thus seen as an inferior limit.

Several observations can be made. First the redeposition is increased with increasing electron temperature. This is not a surprise as the ionisation rate increases with the electron temperature in the $T_e < 100$ eV range. Second the redeposition diminishes with increasing E_{max}/k_BT_e. Redeposition is however only slightly modified above $E_{max}/k_BT_e = 10$ as, except from the fast tail of the Thompson energy distribution, most of the atoms are ejected at an energy of the order of the surface binding energy U_S. At large E_{max}/k_BT_e, all the fast particles manage to exit the sheath, $f_{non-redep}$ being determined by the bulk ions that are only slightly affected by E_{max}/k_BT_e. Third very different non-redeposition fractions could exist in the case of ELMs as it can vary from $\approx 10^{-5}$ at $T_e = 100$ eV to ≈ 1 at $T_e = 1$ eV. Even if the ion impact energy is very large, the magnetised sheath could have still a strong role to play on the redeposition. The possibility of a strong redeposition during ELMs has already been mentioned in [13].

Finally the net erosion due to the self-sputtering of W by W^{12+} is investigated. The effective net sputtering yield is defined as:

$$Y_{net} = f^{sput}_{non-redep} Y(\langle\alpha\rangle) + f^{refl}_{non-redep} \mathrm{Refl}(\langle\alpha\rangle) - 1 \qquad (14)$$

where Refl is the reflection coefficient of W^{12+} on W (data from [31]), 1−Refl being the sticking coefficient. $f^{sput}_{non-redep}$ and $f^{sput}_{non-redep}$ correspond to the non-redeposition fraction of sputtered and reflected W atoms, respectively. As a first approximation, they are taken with the same value and calculated according to the method presented in the current section. The value of Y_{net} is displayed in Figure 14 for the same parameters as Figure 8. Negative values correspond to net deposition. On the right, the contribution of sticking W ions is displayed separately and corresponds to the second and third terms of Equation 14. In the case of the sheath model, the variation of the net erosion under $n_e = 10^{16}$ m^{-3} is negligible when the density is increased. Between $n_e = 10^{16}$ m^{-3} and $n_e = 10^{18}$ m^{-3}, strong variation of the net sputtering is observed as for the gross sputtering (see Figure 8) and is due to the strong modification of the average impact angle in this region (see Figure 6). A similar reduction of the sticking contribution is observed in Figure 14 (right). Above $n_e = 10^{18}$ m^{-3}, the dominant mechanism is redeposition for both the sputtering and sticking contributions leading to a strong decrease of net sputtering and finally to net deposition for $n_e > 10^{19}$ m^{-3}. As a last remark we can observe that the magnetic field angle α_B with respect to the surface has a very moderate effect when the magnetised sheath is considered in comparison to the ballistic model.

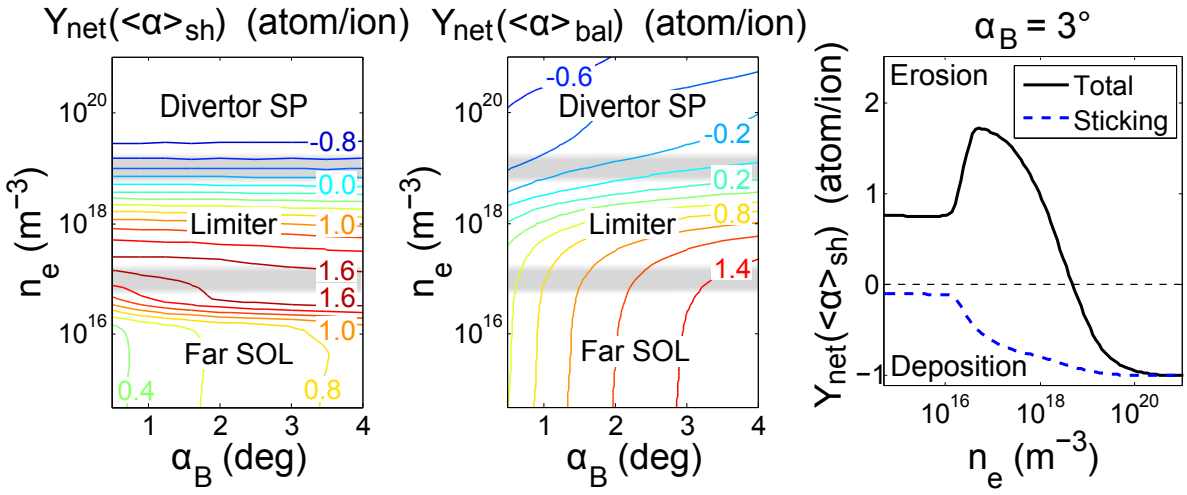


Figure 14. Effective net sputtering yield in the case of the sheath model (left) and of the ballistic model (middle). Right: Effective net sputtering yield for the sheath model at $\alpha_B = 3°$ with the contribution of sticking W ions calculated separately.

6. Discussion about other effects

Several other effects can be discussed. First, collisions are not taken into account in the sheath simulations. To validate this approximation, the distance in the sheath has to be compared with the collisional mean free path. This has for example been performed in [27]. This approximation is valid except at divertor strike points in the case that the

electron density reaches more than 1×10^{20} m^{-3}. This points out the importance to implement a collisional model to investigated those conditions.

ELMs have only been mentioned for redeposition. Concerning the impact angle, no modification is expected with respect to the ballistic model as the ions are extremely energetic leading to a negligible effect of the magnetised sheath on them as the potential drop remains very small in comparison to the ion energy (see Section 5.3).

The third point concerns the treatment of secondary electrons. Even if it is expected that a large part of secondary electrons returns promptly to the surface due the grazing incidence of the magnetic field, it has been shown that for the explanation of some Langmuir probe measurements [41], an emission fraction of 80% of secondary electrons that manage to exit the sheath is required. Their treatment is quite complex as far as their ejection distribution and emission coefficient must be known. Additionally their effect on the sheath potential is hard to simulate as they can stay very close to the surface at a distance much smaller than the Debye length leading to drastic increase of computer resources. A qualitative reasoning can still be made on the basis of the effect that they tend to reduce the magnetised sheath potential drop [19]. In this case, the contribution to the impact energy due to the distribution at the sheath entrance is increased with respect to the contribution of the acceleration inside the magnetised sheath. The error with the traditional assumption $2k_BT_i + 3Zk_BT_e$ can reach a value substantially larger than 20%. Concerning the impact angle, the expected values are situated between the sheath model (without secondary electrons) and the ballistic model. A reduction of the redeposition can also be expected with a lower magnetised sheath potential drop.

7. Conclusion

The magnetised sheath effect has been investigated in the case of impurities for gross erosion and redeposition of tungsten. Three main aspects have been treated. First the energy at the sheath entrance, which is directly correlated to the energy at impact, has been determined using a Vlasov formulation. As expected it increases with charge state, however non-linearly, and it decreases with the mass. The formula obtained differs from the usual $2k_BT_i + 3Zk_BT_e$ approximation. A discrepancy of 20% has been found, which however remains acceptable with respect to other uncertainties like sputtering yields. The self-consistently calculated sheath electric field of a D plasma has then been used to calculate the average impact angle of impurities and the underlying redeposition of W atoms.

Second the impact angle has been computed: it exhibits a stronger effect of the sheath for impurities than for the main species. Two cases can be distinguished. At low density ions are mainly accelerated along the magnetic field line and this leads to a decrease of the impact angle by the sheath. At large density the ions are strongly accelerated toward the wall during their last gyration leading to an increase of the impact angle. Those mechanisms have been validated considering the dependence of those two cases with the charge state and the mass. The difference in impact angle can

lead to a strong difference in the effective sputtering yield of impurities. In particular for W^{12+} impinging W, a discrepancy of 3-4 times can be observed for large density and small angle with respect to the ballistic model. This depends however on the sputtering yield angular dependence.

Third local redeposition has been investigated and the way how to calculate a correction factor on the impurity flux for edge transport codes. Two cases have been distinguished: the ejected atoms whose velocity projected on **B** is oriented towards the wall and towards the plasma. In the first case, redeposition depends on the sheath width. The optimal simulation domain extends until where the impinging ions are injected: $L_{simu} = 10\sqrt{2(1+1\zeta^2)}\lambda_D$, provided that edge codes consider this region out of their simulation domain. In the second case, redeposition depends on the sheath electric field, which is not considered in edge codes, and a simulation domain of $L_{simu} = 20\sqrt{2(1+\zeta^2)}\lambda_D$ is required to capture all effects. The sheath is finally shown to increase strongly prompt redeposition in comparison to the long-range contributions that disappears almost totally at large electron densities.

References

[1] Gunn J P 1997 *Phys. Plasmas* **4** 4435
[2] Eckstein W 2007 *Sputtering by Particle Bombardment* (*Topics in Applied Physics* vol 110) (Springer Berlin Heidelberg) 33-187
[3] Mellet N, Martin C, Pégourié B, et al 2014 *Nucl. Fusion* **54** 123006
[4] Schmid K, Mayer M, Adelhelm C, et al 2010 *Nucl. Fusion* **50** 105004
[5] Kawamura G, Tomita Y and Kirschner A 2013 *J. Nucl. Mater.* **438** S909
[6] Devaux S and Manfredi G 2008 *Plasma Phys. Control. Fusion* **50** 025009
[7] Stangeby P C 2012 *Nucl. Fusion* **52** 083012
[8] Borodkina I E, Komm M and Tsvetkov I V 2015 *Russian Physics Journal* **58** 438
[9] Kirschner A, Philipps V, Winter J and Kögler U 2000 *Nucl. Fusion* **40** 989
[10] Brooks J N 2002 *Fusion Eng. Des.* **60** 515
[11] Naujoks D, Asmussen K, Bessenrodt-Weberpals M, et al 1996 *Nuclear Fus.* **36** 671
[12] Kirschner A, Tskhakaya D, Kawamura G, et al 2016 *Contrib. Plasma Phys.* **56** 622
[13] Chankin A V, Coster D P and Dux R 2014 *Plasma Phys. Control. Fusion* **56** 025003
[14] Brooks J N 1990 *Phys. Fluids B* **2** 1858
[15] Tskhakaya D, Groth M, et al 2015 *J. Nucl. Mater.* **463** 624
[16] Bufferand H, Ciraolo G, Marandet Y, et al 2015 *Nucl. Fusion* **55** 053025
[17] Dai S, Wang L, Kirschner A, et al 2015 *Nucl. Fusion* **55** 043003
[18] van Rooij G J,Coenen J W, Aho-Mantila L, et al 2013 *J. Nucl. Mater.* **438** S42
[19] Stangeby P 2000 *The Plasma Boundary of Magnetic Fusion Devices* (Institute of Physics Publishing, London)
[20] Bohm D 1949 *The Characteristics of Electrical Discharges in Magnetic Fields ed A Guthrie and R K Wakerling* (New York: McGraw-Hill)
[21] Kočan M and Gunn J P 2011 *Plasma Phys. Control. Fusion* **53** 085016
[22] Chung K S and Hutchinson I H 1988 *Phys. Rev. A* **38** 4721
[23] Thompson M W 1968 *Philos. Mag.* **18** 377
[24] Goehlich A, Niemöller N and Döbele H F 1999 *J. Nucl. Mater.* **266-269** 501
[25] Yalin A P, Williams J D, Surla V and Zoerb K A 2007 *J. Phys. D: Appl. Phys.* **40** 3194
[26] Stepanova M and Dew S K 2003 *Nucl. Instrum. Methods Phys. Res., Sect. B* **215** 357
[27] N. Mellet, B. Pégourié, C. Martin et al 2016 *Phys. Scr.* **T167** 014064

[28] Mousel T, Eckstein W and Gnaser H 1999 *Nucl. Instr. Meth. Phys. Res. B* **152** 36
[29] Yamamura Y, Bohdansky J 1985 *Vacuum* **35** 561
[30] http://open.adas.ac.uk/
[31] Eckstein W 2002 *Calculated Sputtering, Reflection and Range Values* IPP 9/132
[32] Bufferand H, Ciraolo G, Isoardi L, et al 2011 *J. Nucl. Mater.* **415** S589
[33] Rozhansky V A, Voskoboynikov S P, Kaveeva E G, et al 2001 *Nucl. Fusion* **41** 387
[34] Radford G J, Chankin A V, Corrigan G, et al 1996 *Contrib. Plasma Phys.* **36** 187
[35] Reiter D, Baelmans M, Boerner P 2005 *Fusion Sci. Technol.***47** 172
[36] Marandet Y, Bufferand H, Bucalossi 2015 *J. Nucl. Mater.***463** 629
[37] Guillemaut C, Jardin A, Horacek J et al 2016 *Phys. Scr.***T167** 014005
[38] Fundamenski W, Pitts R A 2006 *Plasma Phys. Control. Fus.* **48** 109
[39] Moulton D, Fundamenski W, Manfredi G, et al 2013 *J. Nucl. Mater.* **438** S633
[40] Pitts R A, Alberti S, Blanchard P, et al 2003 *Nucl. Fusion* **43** 1145
[41] Gunn J P 2012 *Plasma Phys. Control. Fus.* **54** 085007